Supplementary Information

Unexpected Presence of Alkali Metal Cation Impurities, Stabilizing Cu^+ in Oxide-Derived Cu for CO_2 Electrolysis

Haesol Kim,[1,†] Seunghoon Lee,[1,†] Jihoon Son,[2,†] Hansol Choi,[1] Junsic Cho,[1] Baptiste Gault,[3,4] Won-Hyoung Lee,[5] Benedikt Paul Klein,[6] Cheolho Jeon,[6] Joonhee Moon,[6] Da Hye Won,[7,8] Dae-Hyun Nam,[5] Gyeongwon Kang,[9] Hyeyoung Shin,[2,*] Se-Ho Kim,[3,5,*] and Chang Hyuck Choi[1,*]

[1]Department of Chemistry, Pohang University of Science and Technology (POSTECH), Pohang 37673, Republic of Korea.

[2]Graduate School of Energy Science and Technology, Chungnam National University, Daejeon 34134, Republic of Korea.

[3]Max Planck Institute for Sustainable Materials, 40237 Düsseldorf, Germany.

[4]Department of Materials, Imperial College London, Exhibition Road, London SW7 2AZ, U.K.

[5]Department of Materials Science and Engineering, Korea University, Seoul 02841, Republic of Korea.

[6]Research Center for Materials Analysis, Korea Basic Science Institute (KBSI), Daejeon 34133, Republic of Korea.

[7]Clean Energy Research Center, Korea Institute of Science and Technology (KIST), Seoul 02792, Republic of Korea.

[8]KHU-KIST Department of Converging Science and Technology, Kyung Hee University, Seoul 02477, Republic of Korea.

[9]Department of Chemistry, Kangwon National University, Chuncheon 24341, Republic of Korea.

[†]These authors contributed equally.

*Corresponding authors: (H.S.) shinhy@cnu.ac.kr, (S.-H.K.) sehonetkr@korea.ac.kr, and (C.H.C.) chchoi@postech.ac.kr

Supplementary Note 1 | Physical and electrochemical properties of OD_{Li}-Cu and OD_{Cs}-Cu samples

In addition to OD_{Na}-Cu, we also prepared OD_{Li}-Cu and OD_{Cs}-Cu by electrochemical reduction of the Cu oxide film at 7.5 mA cm^{-2} in CO_2-saturated 0.1 M $LiHCO_3$ and $CsHCO_3$ electrolytes, respectively. X-ray diffraction (XRD) patterns of OD_{Li}-Cu and OD_{Cs}-Cu displayed dominant metallic Cu signals at 43, 51, and 74° (Supplementary Fig. 6). X-ray photoelectron spectroscopy (XPS) spectra revealed a red-shifted Cu $2p_{3/2}$ peak at 932.7 eV after electroreduction. Roughened surface morphologies with roughness factors (R_q) of 32.3 and 35.6 nm were identified by scanning electron microscopy (SEM) and atomic force microscopy (AFM) images. Besides, cryogenic atom probe tomography (cryo-APT) analyses of OD_{Li}-Cu and OD_{Cs}-Cu confirmed the presence of residual oxygen after electroreduction of Cu oxide (Supplementary Figs. 7–8 and Supplementary Table 1). Notably, non-negligible amounts of Li^+ (0.235 ± 0.003 at.%) and Cs^+ (0.585 ± 0.003 at.%) were detected in OD_{Li}-Cu and OD_{Cs}-Cu, respectively. APT mapping unveiled that these alkali metal cation (AM^+) impurities are preferentially concentrated on certain areas, similar to the case of OD_{Na}-Cu. In CO_2 electrolysis, performed in a CO_2-saturated 0.1 M $NaHCO_3$ to avoid electrolyte effect,[1-3] both OD_{Li}-Cu and OD_{Cs}-Cu exhibited higher initial CO_2 reduction reaction (CO_2RR) activities compared to m-Cu (Supplementary Fig. 9). At −0.5 V_{RHE}, OD_{Li}-Cu and OD_{Cs}-Cu showed high CO partial current density (j_{CO}; 0.60 and 0.66 mA cm^{-2}, respectively) and Faradaic efficiency (FE_{CO}; 23 and 25%, respectively) with suppressed hydrogen evolution reaction (HER) selectivity, comparable to those for OD_{Na}-Cu. A similar trend was also observed for C_2H_4 production at −1.0 V_{RHE}. Hence, these results confirmed that OD_{Li}-Cu and OD_{Cs}-Cu shared similar physical properties with OD_{Na}-Cu and exhibited better CO_2RR selectivity than m-Cu, indicating that AM^+ incorporation is a universal event accompanying a significant phase transition during Cu oxide electroreduction.

Supplementary Note 2 | Enhanced CO_2RR activity in $NaHCO_3$ compared to $TBAHCO_3$ electrolyte.

In the pulsed electrolysis of CO_2, we employed two different electrolytes, $NaHCO_3$ and $TBAHCO_3$, to study the dynamic formation and leaching of Na^+-containing microstructures during the reaction. However, it is important to note that the identity of the cation species (Na^+ *vs*. TBA^+) in the electrolyte can influence the CO_2RR performance—a phenomena widely known as the "cation effect", whose fundamental origin remains under active debate.[1,4] Consistent with the previous reports,[5,6] OD_{Na}-Cu exhibited higher CO_2RR activity in $NaHCO_3$ than in $TBAHCO_3$, with initial j_{CO} values of approximately 0.5 and 0.3–0.2 mA cm^{-2} during 1 h of operation (Fig. 2f,g), respectively. Control experiments under potentiostatic polarization at −0.5 V_{RHE} further confirmed this trend (Supplementary Fig. 24): OD_{Na}-Cu showed an initial j_{CO} of 0.7 mA cm^{-2} in $NaHCO_3$, compared to 0.3 mA cm^{-2} in $TBAHCO_3$. Similarly, OD_{TBA}-Cu, which lacked Na^+-containing microstructures, also displayed a higher initial j_{CO} in $NaHCO_3$ (0.2 mA cm^{-2}) than in $TBAHCO_3$ (0.1 mA cm^{-2}). Note that the electrolyte pH, which could otherwise influence electron transfer kinetics,[7] remained nearly identical for both CO_2-saturated 0.1 M $NaHCO_3$ and $TBAHCO_3$ solutions (pH ≈ 6.7). Therefore, the observed differences in CO_2RR activity in different electrolytes can be attributed, at least in part, to the conventional cation effects. Nevertheless, we emphasize that the higher CO_2RR performance of OD_{Na}-Cu compared to OD_{TBA}-Cu, measured in an identical electrolyte, cannot be explained by the conventional cation effect, highlighting the critical role of dynamically generated Na^+-containing microstructures in promoting CO_2RR.

Supplementary Figures

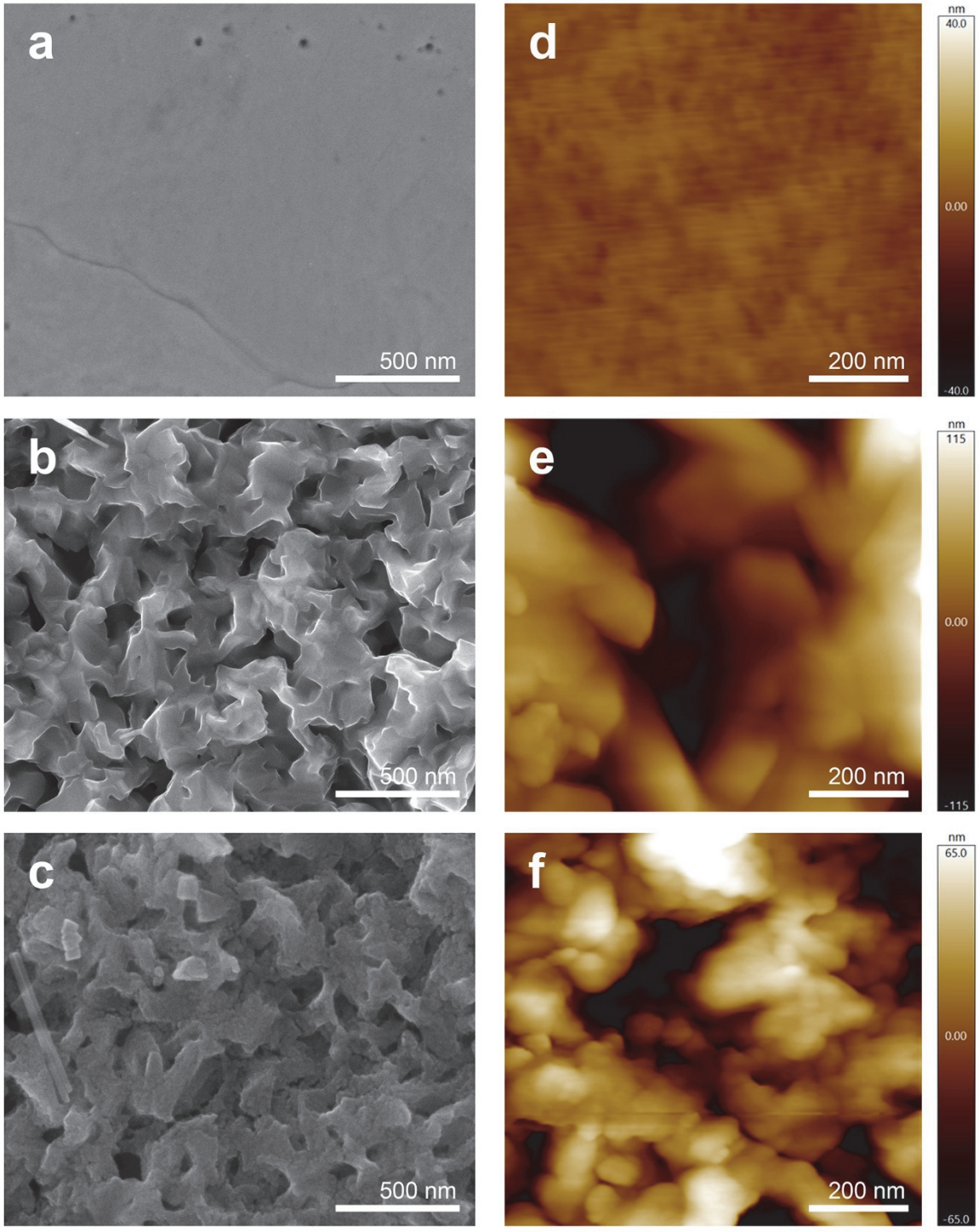

Supplementary Fig. 1 | Surface morphology of m-Cu, Cu oxide, and as-prepared OD_{Na}-Cu. a–c, SEM and **d–f**, AFM images of m-Cu (**a,d**), Cu oxide (**b,e**), and as-prepared OD_{Na}-Cu (**c,f**).

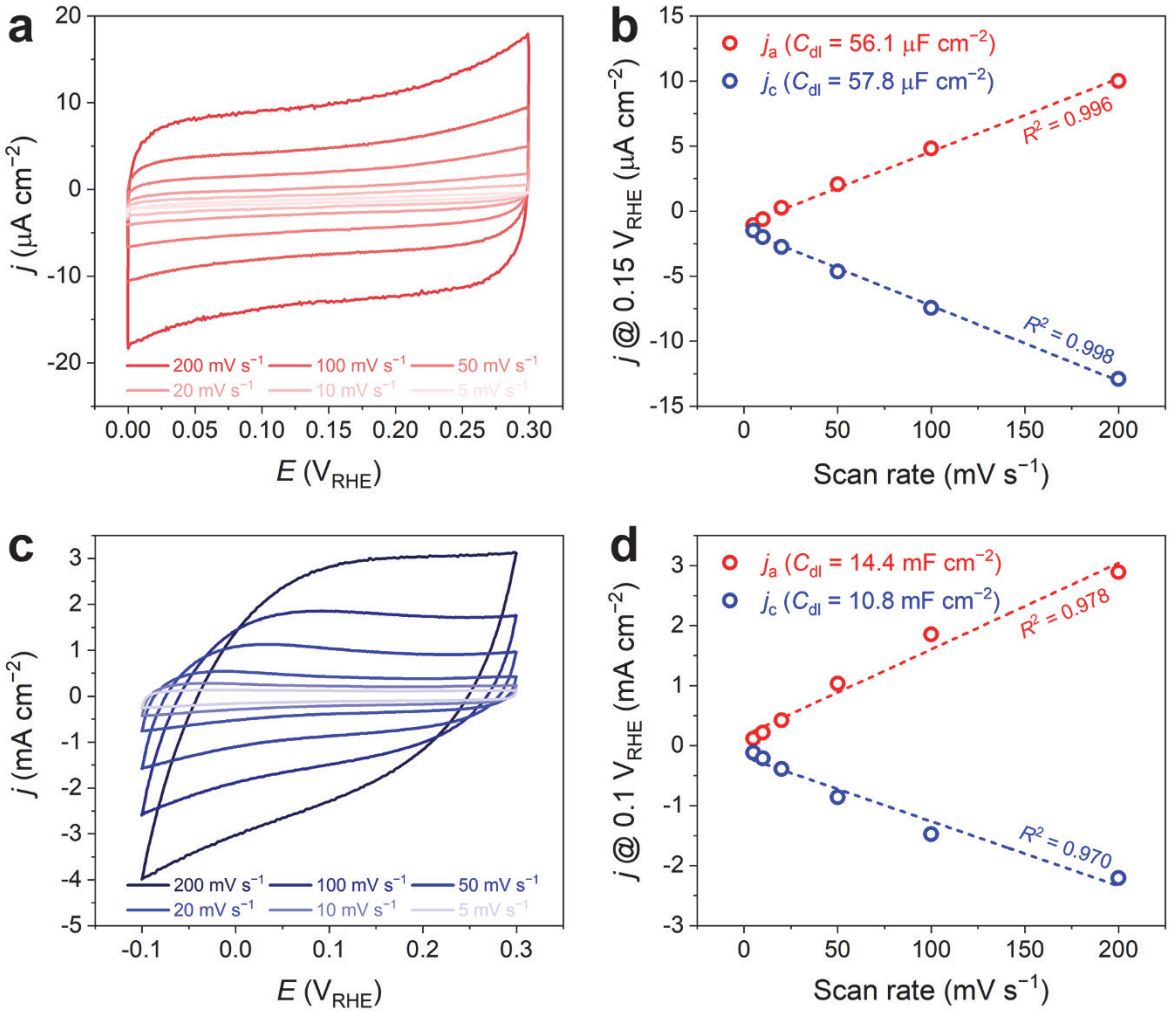

Supplementary Fig. 2 | Capacitive responses. Cyclic voltammetry (CV) responses of **a**, m-Cu and **c**, OD_{Na}-Cu measured at scan rates of 5–200 mV s^{-1}. Corresponding plots of capacitive *j vs*. scan rate for **b**, m-Cu and **d**, OD_{Na}-Cu. The estimated double-layer capacitance (C_{dl}) values are approximately 57.0 μF cm^{-2} and 12.6 mF cm^{-2} for m-Cu and OD_{Na}-Cu, respectively.

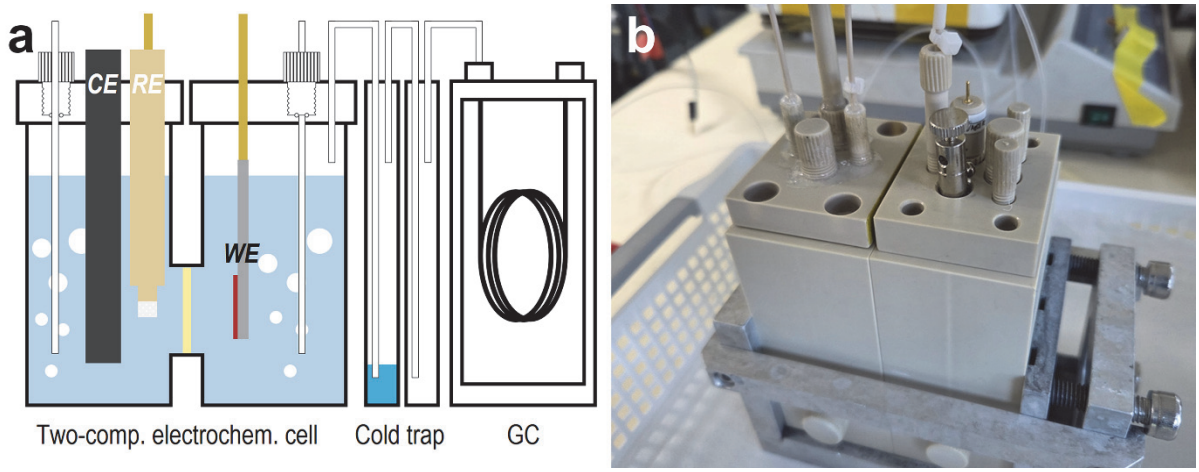

Supplementary Fig. 3 | Electrochemical cell used for CO_2RR studies. a, Schematic and **b**, photographic images of the two-compartment cell coupled to the online gas chromatography (GC) system.

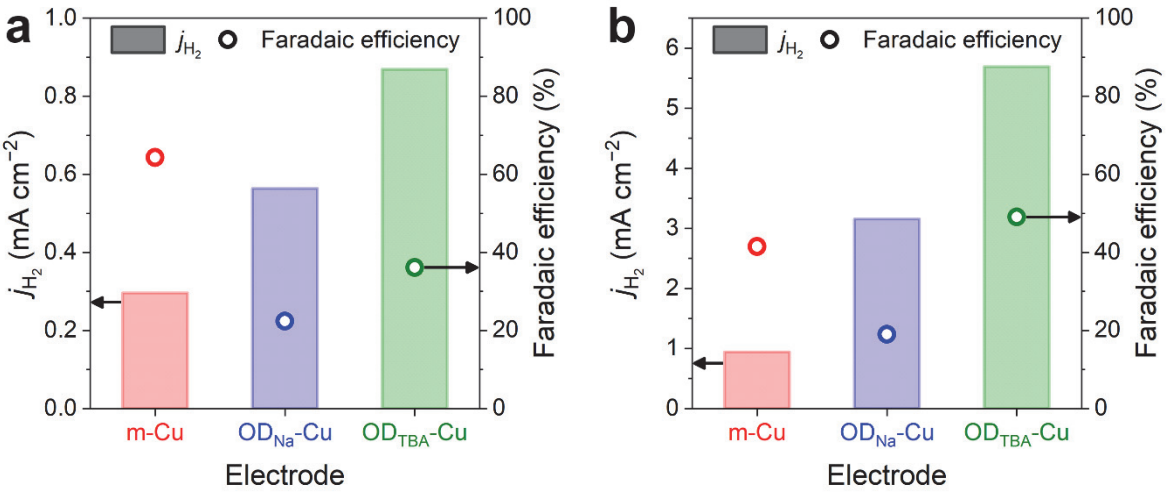

Supplementary Fig. 4 | H_2 production rates. Initial partial current densities and Faradaic efficiencies for H_2 production on m-Cu, OD_{Na}-Cu, and OD_{TBA}-Cu at **a**, −0.5 and **b**, −1 V_{RHE} in a CO_2-saturated 0.1 M $NaHCO_3$ electrolyte.

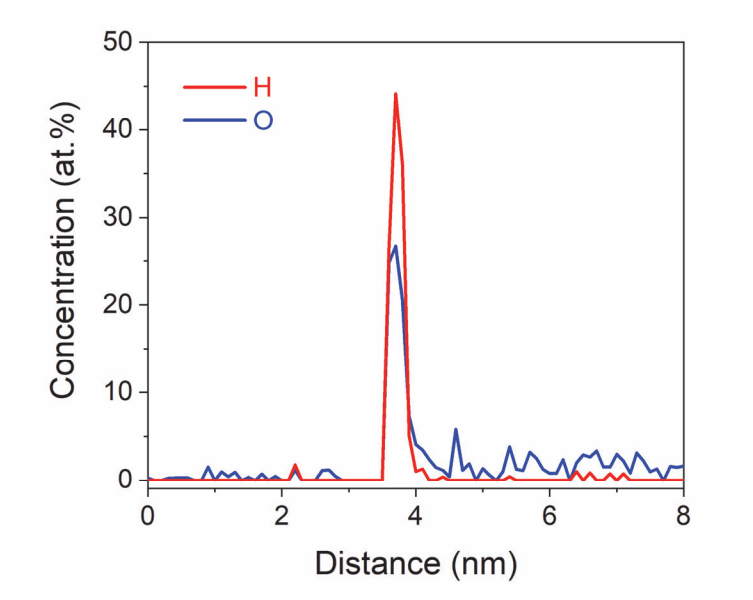

Supplementary Fig. 5 | Atomic composition in the water-filled nanopore of OD_{Na}-Cu. The observed H:O atomic ratio was approximately 2:1, inferring the presence of water in the OD-Cu matrix as the water-filled nanopores.

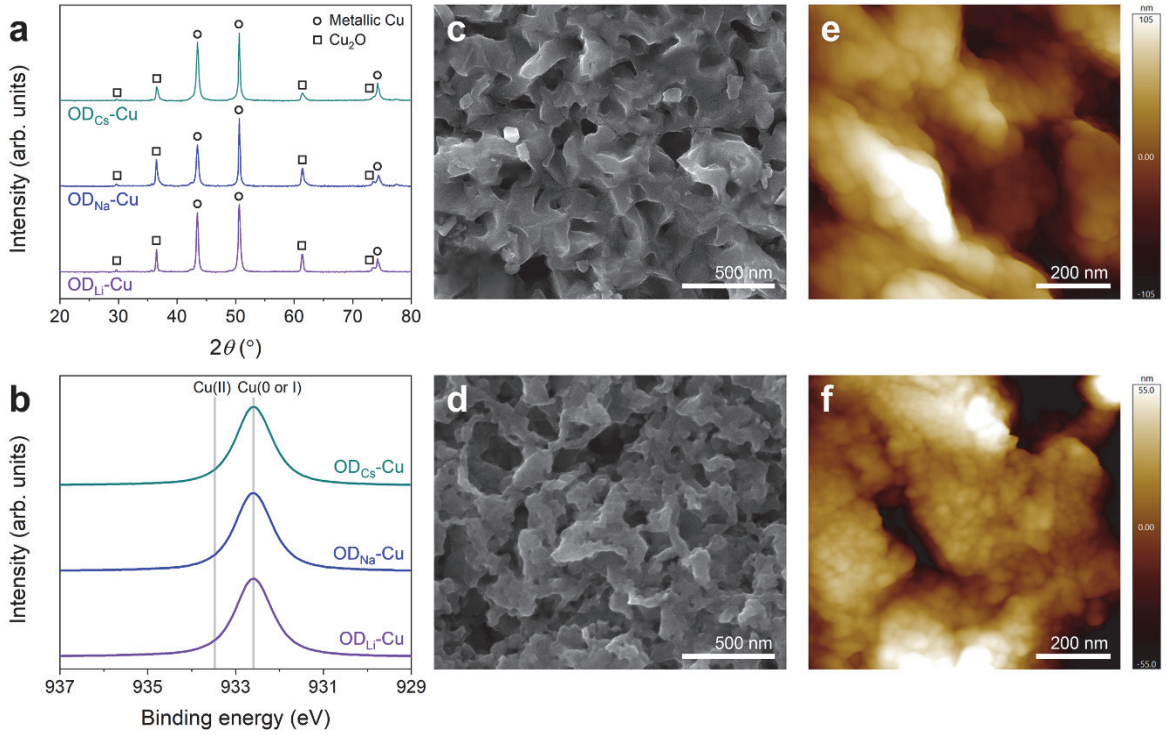

Supplementary Fig. 6 | Physical characterization of OD_{Li}-Cu and OD_{Cs}-Cu. a, XRD patterns and **b**, XPS Cu $2p_{3/2}$ spectra of OD_{Li}-Cu and OD_{Cs}-Cu. For comparison, data for OD_{Na}-Cu are also included. **c,d**, SEM and **e,f**, AFM images of OD_{Li}-Cu (**c,e**) and OD_{Cs}-Cu (**d,f**).

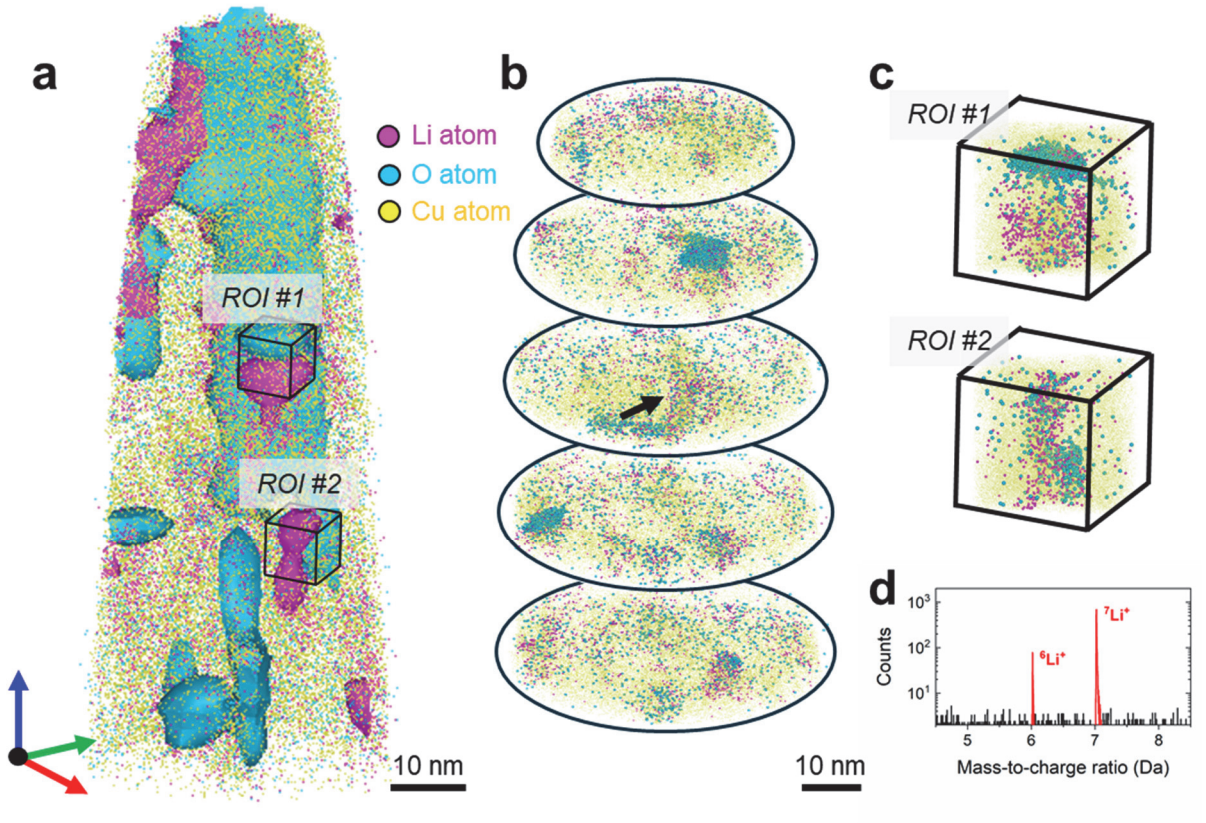

Supplementary Fig. 7 | Cryo-APT analysis of OD_{Li}-Cu. a, Ion map histogram and **b**, corresponding 3 nm-thick sliced tomograms. **c**, Extracted cuboidal atom map of region of interest (ROI; 10×10×10 nm^3), showing the Li:Cu:O ratio as 0.6:96.6:2.8 (ROI #1) and 0.4:97.8:1.8 (ROI #2), respectively. **d**, Mass spectrum for OD_{Li}-Cu, indicating the presence of Li^+ impurities (m/z = 6 and 7).

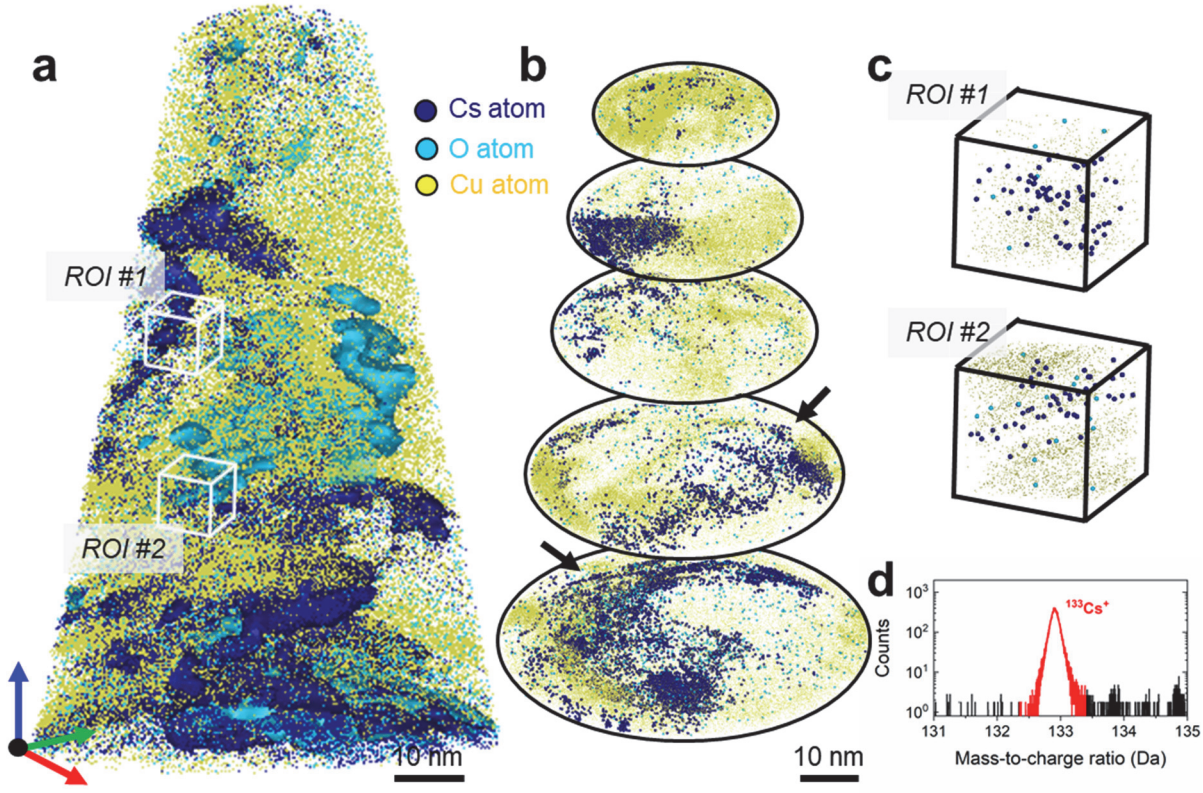

Supplementary Fig. 8. | Cryo-APT analysis of OD_{Cs}-Cu. a, Ion map histogram and **b**, corresponding 3 nm-thick sliced tomograms. **c**, Extracted cuboidal atom map of ROI (10×10×10 nm^3), showing the Cs:Cu:O ratio as 5.3:93.0:1.7 (ROI #1) and 1.1:94.4:4.5 (ROI #2), respectively. **d**, Mass spectrum for OD_{Cs}-Cu, indicating the presence of Cs^+ impurities (m/z = 133).

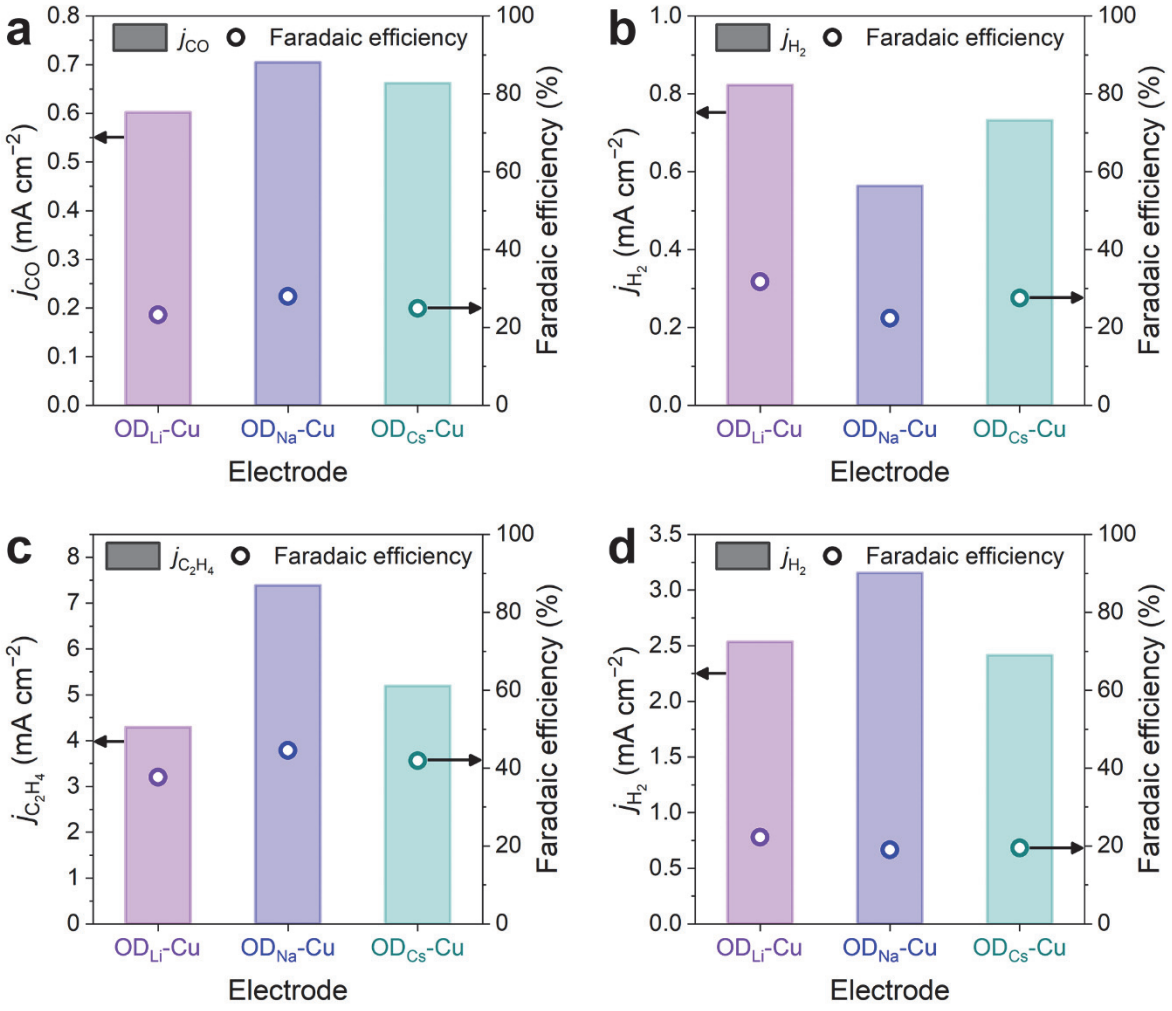

Supplementary Fig. 9 | Initial CO_2RR performance of OD_{Li}-Cu and OD_{Cs}-Cu. Initial partial current densities and Faradaic efficiencies for **a**, CO and **b**, H_2 production on OD_{Li}-Cu and OD_{Cs}-Cu at −0.5 V_{RHE}, and for **c**, C_2H_4 and **d**, H_2 production on OD_{Li}-Cu and OD_{Cs}-Cu at −1 V_{RHE}. The electrolyte was a CO_2-saturated 0.1 M $NaHCO_3$. For comparison, data for OD_{Na}-Cu are also included.

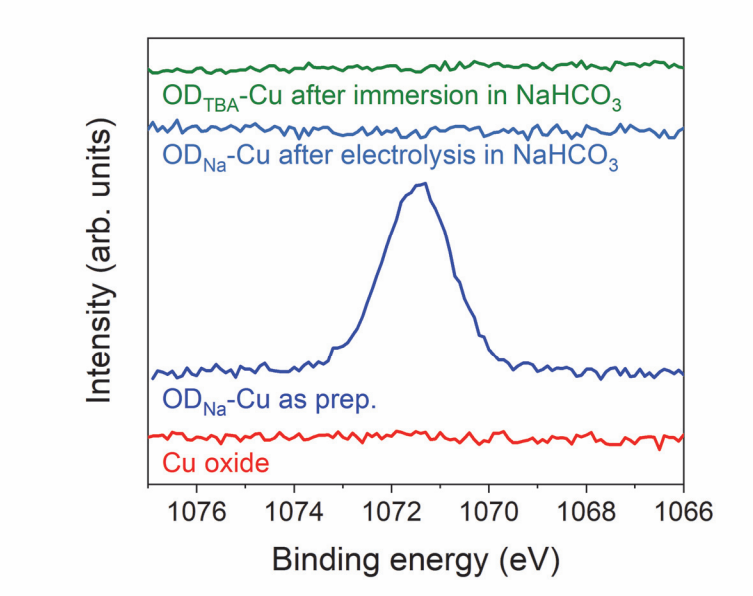

Supplementary Fig. 10 | XPS Na 1*s* spectra of Cu oxide, as-prepared OD$_{Na}$-Cu, OD$_{Na}$-Cu after CO$_2$ electrolysis, and OD$_{TBA}$-Cu after immersion in NaHCO$_3$ electrolyte. Cu oxide shows no detectible Na^+ signal, whereas as-prepared OD$_{Na}$-Cu exhibits a clear Na 1*s* peak at 1071.5 eV (*i.e.*, Na^+). After CO_2 electrolysis at −0.5 V_{RHE} for 6 h in a CO_2-saturated 0.1 M $NaHCO_3$ electrolyte, however, the Na 1*s* signal becomes undetectable. These results indicate that *Na^+ impurities in OD$_{Na}$-Cu, as identified in the bulk by cryo-APT study, are also present near the electrode surface*, and that the Na^+-containing microstructures are highly unstable under CO_2RR conditions. The disappearance of the Na 1*s* signal after electrolysis further confirms that *the peak at 1071.5 eV observed in the as-prepared OD$_{Na}$-Cu is not due to residual electrolyte contamination, but originates from Na^+ impurities within the microstructures* that remained even after washing with deionized (DI) water. In addition, the Na^+-free control sample, *i.e.*, OD$_{TBA}$-Cu, shows no evidence of Na^+ incorporation even after immersion in $NaHCO_3$ electrolyte, further excluding residual electrolyte contamination.

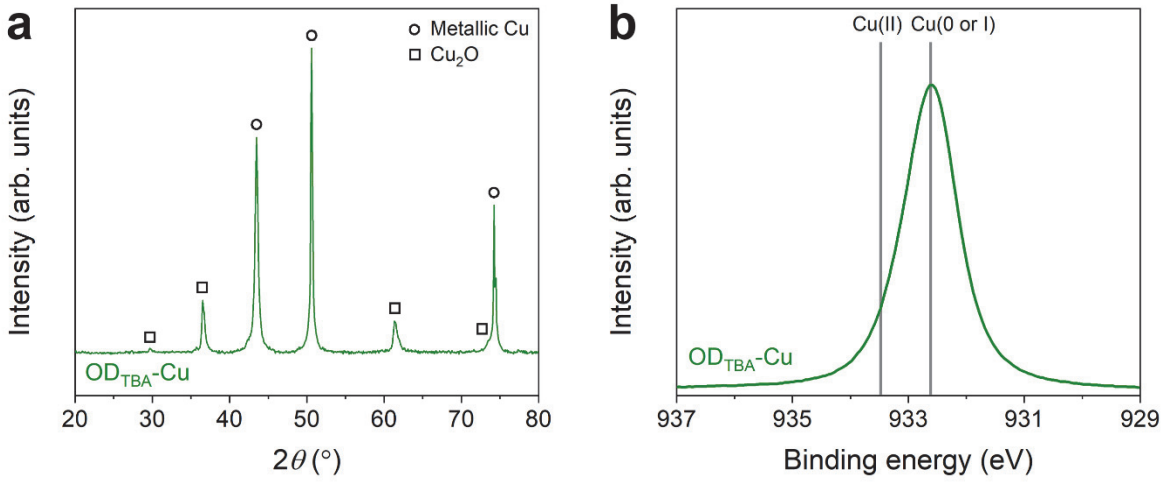

Supplementary Fig. 11 | Physical characterization of as-prepared OD_{TBA}-Cu. a, XRD pattern and **b**, XPS Cu $2p_{3/2}$ spectrum of OD_{TBA}-Cu. OD_{TBA}-Cu exhibits comparable characteristics to OD_{Na}-Cu, showing a dominant metallic Cu signal in XRD pattern and a red-shifted Cu $2p_{3/2}$ peak at 932.7 eV in the XPS spectrum.

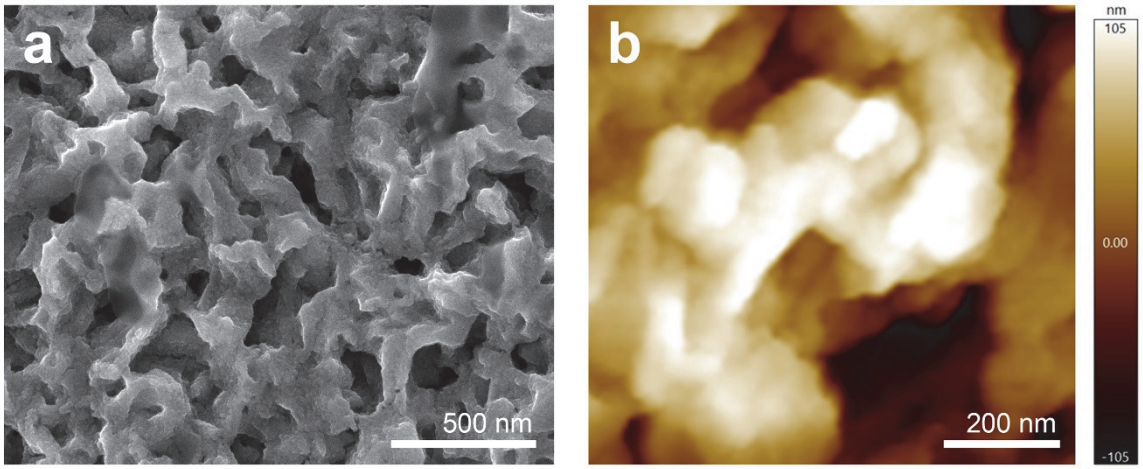

Supplementary Fig. 12. | Surface morphology of as-prepared OD_{TBA}-Cu. a, SEM and **b**, AFM images of as-prepared OD_{TBA}-Cu. A roughened surface morphology with a roughness factor of 39.1 nm is observed, similar to that of OD_{Na}-Cu.

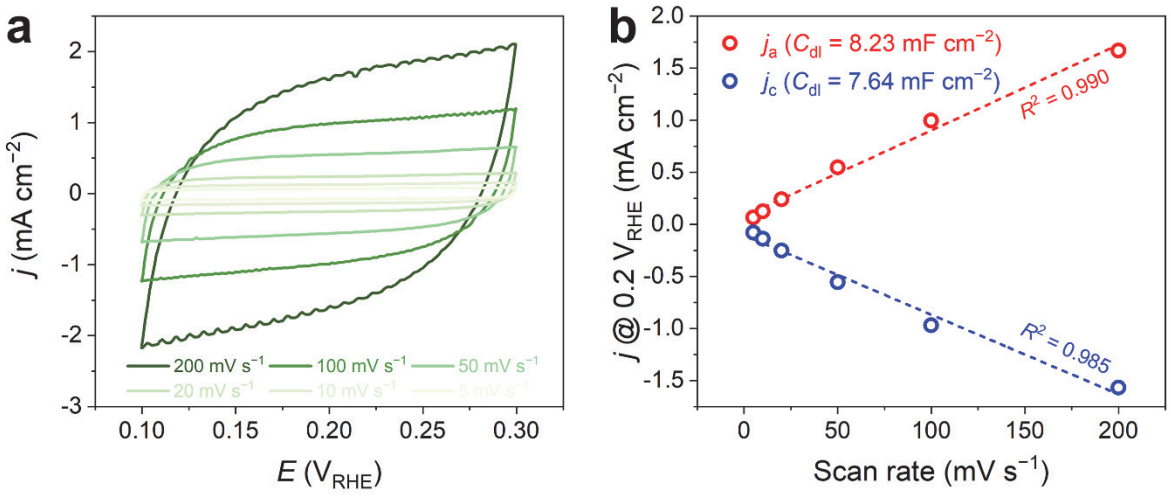

Supplementary Fig. 13 | Capacitive responses of OD_{TBA}-Cu. a, CV responses of OD_{TBA}-Cu measured at scan rates of 5–200 mV s^{-1}. **b**, Corresponding plots of capacitive *j vs*. scan rate. The estimated C_{dl} values are approximately 7.94 mF cm^{-2}, indicating an enlarged surface area after the electroreduction of Cu oxide in $TBAHCO_3$ electrolyte, similar to the behavior observed in $NaHCO_3$.

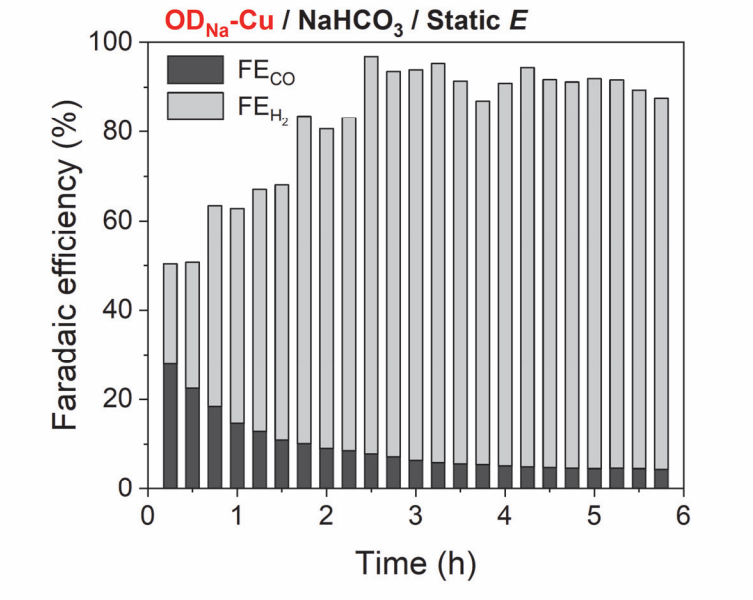

Supplementary Fig. 14 | Stability test at a constant potential of −0.5 V_{RHE}. Faradaic efficiencies for CO and H_2 production on OD_{Na}-Cu for 6 h CO_2RR operation at −0.5 V_{RHE} in a CO_2-saturated 0.1 M $NaHCO_3$ electrolyte.

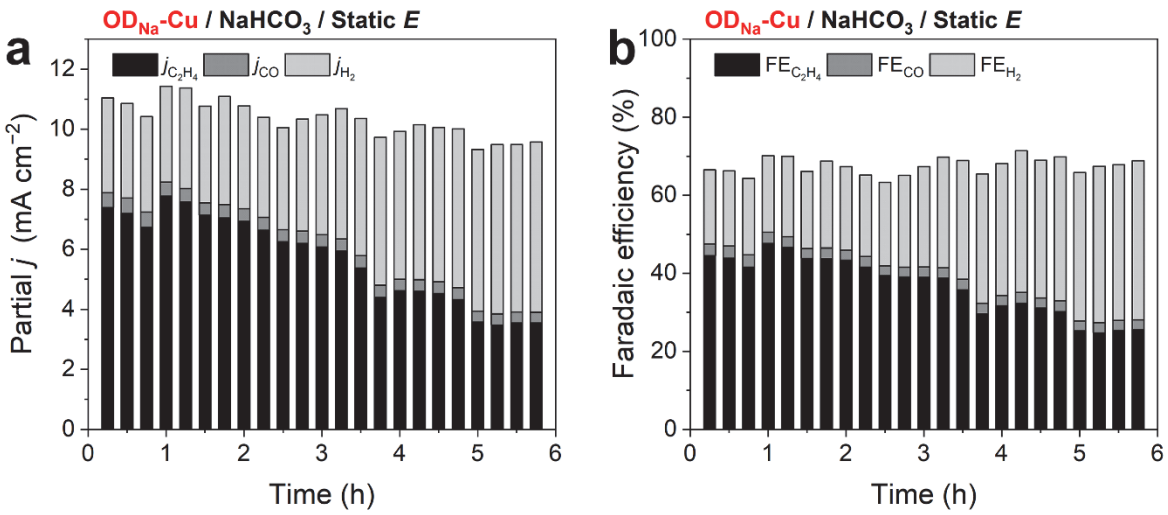

Supplementary Fig. 15 | Stability test at a constant potential of −1 V_{RHE}. a, Partial current densities and **b**, Faradaic efficiencies for C_2H_4, CO, and H_2 production on OD_{Na}-Cu for 6 h CO_2RR operation at −1 V_{RHE} in a CO_2-saturated 0.1 M $NaHCO_3$ electrolyte.

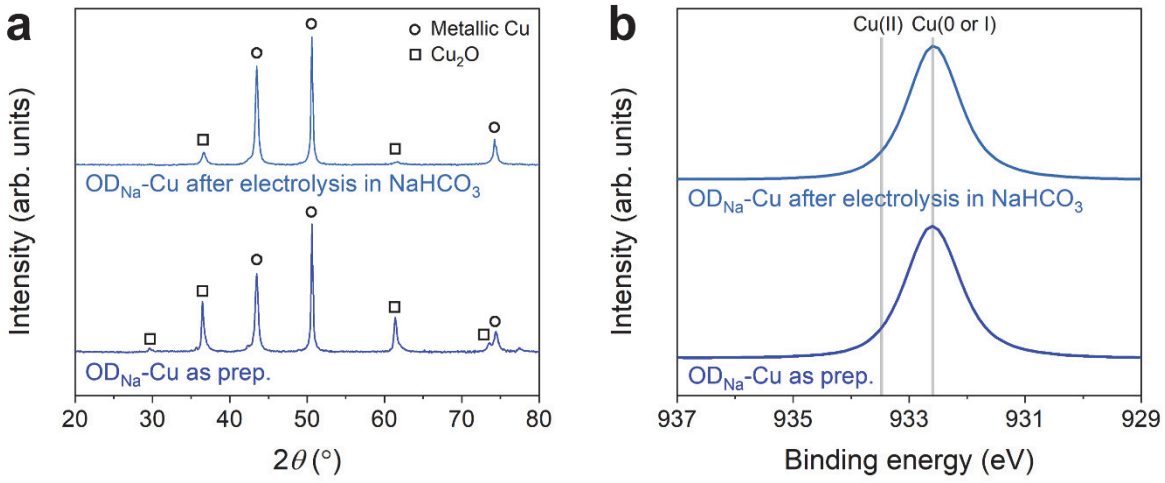

Supplementary Fig. 16 | Physical characterization of OD_{Na}-Cu after stability test. a, XRD pattern and **b**, XPS Cu $2p_{3/2}$ spectrum of OD_{Na}-Cu after 6 h CO_2RR operation at −0.5 V_{RHE} in a CO_2-saturated 0.1 M $NaHCO_3$ electrolyte. For comparison, data for as-prepared OD_{Na}-Cu are also included. The results show that OD_{Na}-Cu after the CO_2RR operation retains comparable characteristics to the as-prepared sample, exhibiting a dominant metallic Cu signal in XRD pattern and a Cu $2p_{3/2}$ peak at 932.7 eV in the XPS spectrum.

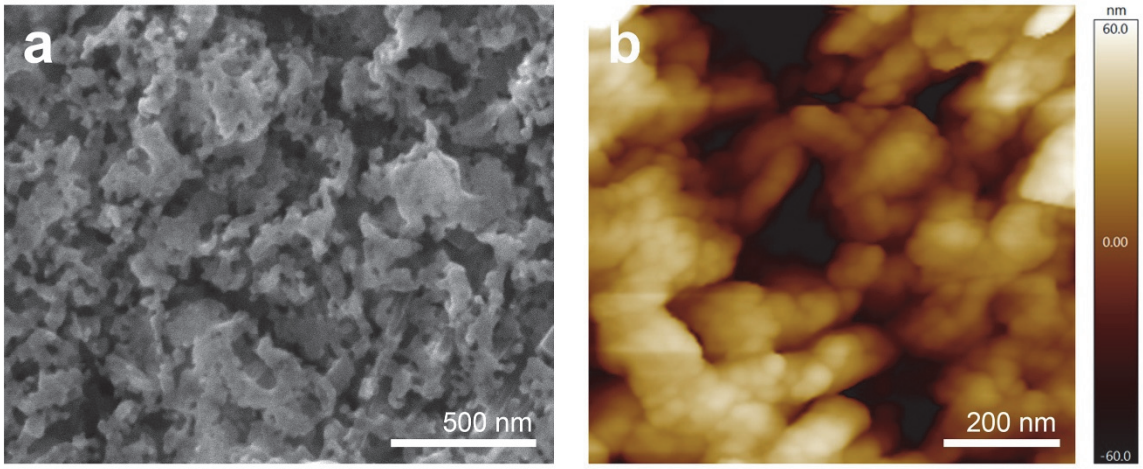

Supplementary Fig. 17 | Surface morphology of OD_{Na}-Cu after stability test. a, SEM and **b**, AFM images of OD_{Na}-Cu after 6 h CO_2RR operation at −0.5 V_{RHE} in a CO_2-saturated 0.1 M $NaHCO_3$ electrolyte. A roughened surface morphology with a roughness factor of 29.2 nm is observed, similar to that of as-prepared OD_{Na}-Cu.

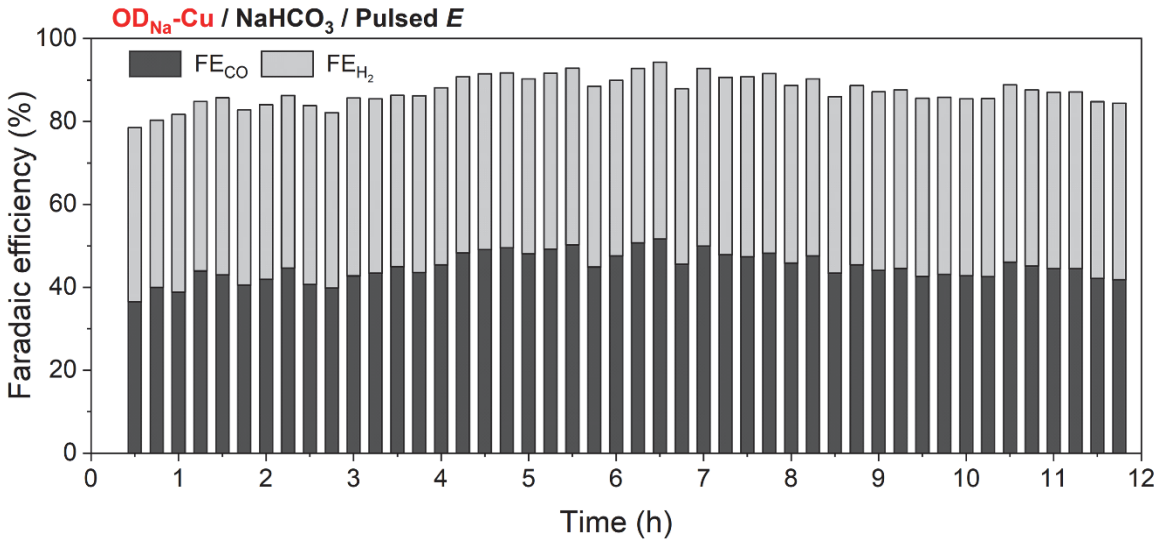

Supplementary Fig. 18 | Pulsed electrolysis of CO_2 to CO on OD_{Na}-Cu. Faradaic efficiencies for CO and H_2 production on OD_{Na}-Cu for 12 h pulsed electrolysis between 0.6 (3 s) and −0.5 (7 s) V_{RHE} in a CO_2-saturated 0.1 M $NaHCO_3$ electrolyte.

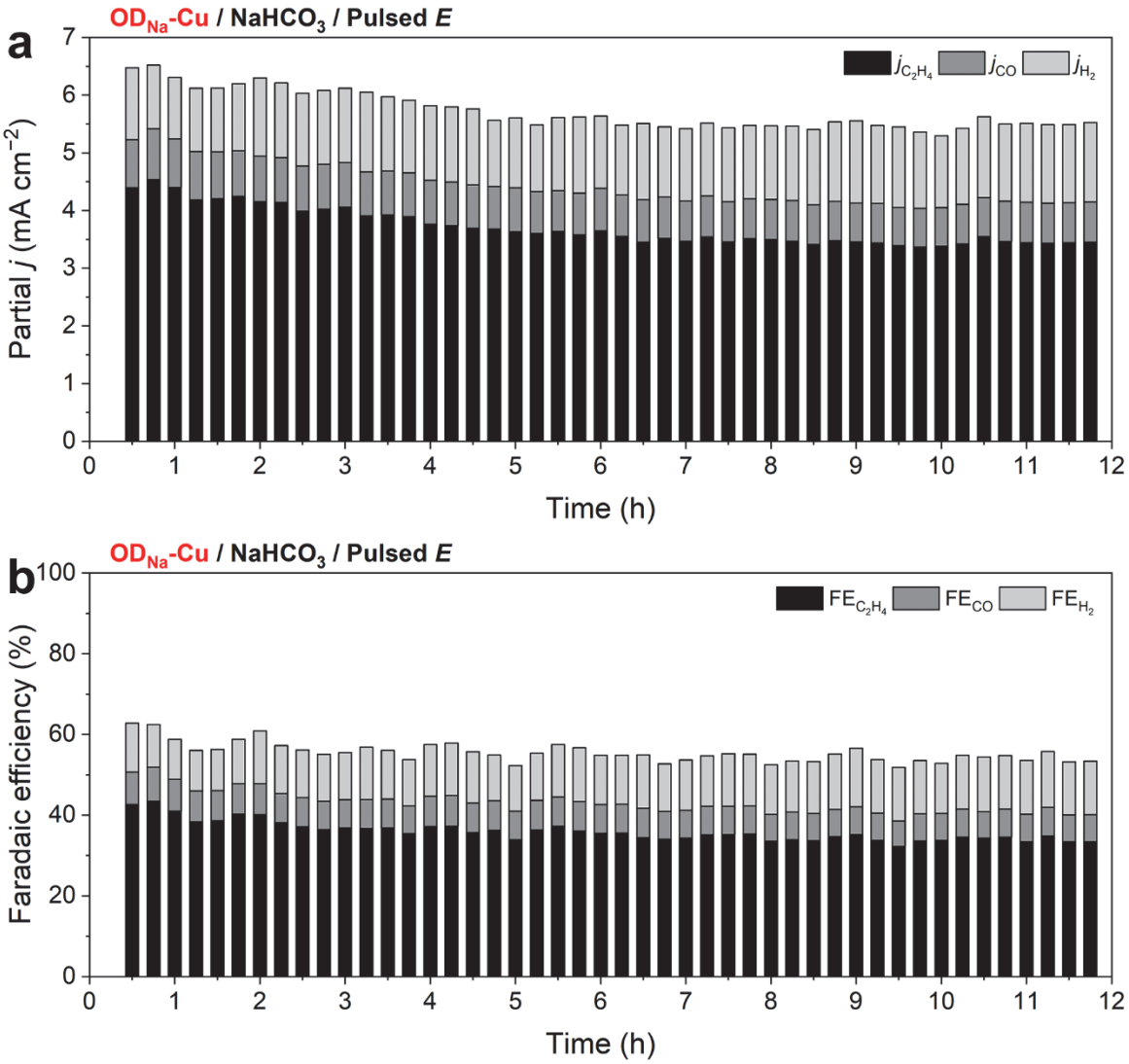

Supplementary Fig. 19 | Pulsed electrolysis of CO_2 to C_2H_4 on OD_{Na}-Cu. a, Partial current densities and **b**, Faradaic efficiencies for C_2H_4, CO, and H_2 production on OD_{Na}-Cu for 12 h pulsed electrolysis between 0.6 (3 s) and −1 (7 s) V_{RHE} in a CO_2-saturated 0.1 M $NaHCO_3$ electrolyte.

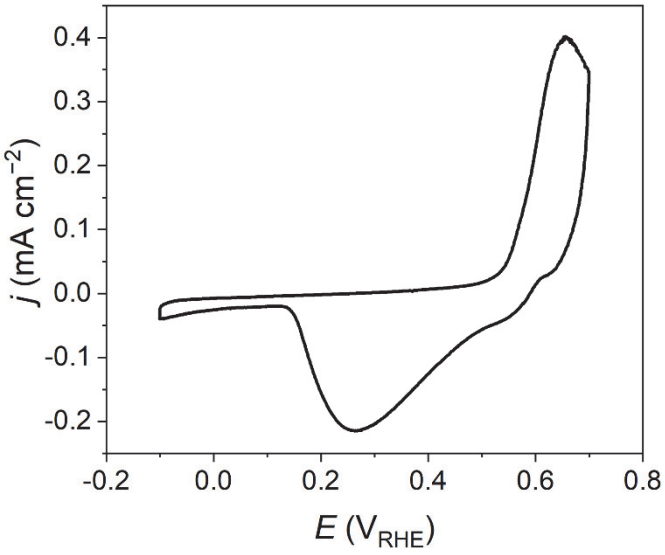

Supplementary Fig. 20 | Phase transition of Cu. CV response of m-Cu measured at a scan rate of 50 mV s^{-1} in an Ar-saturated 0.1 M $NaHCO_3$ electrolyte. The result shows that Cu oxidation starts at a potential below 0.6 V_{RHE} and that its reduction peaks at approximately 0.25 V_{RHE}.

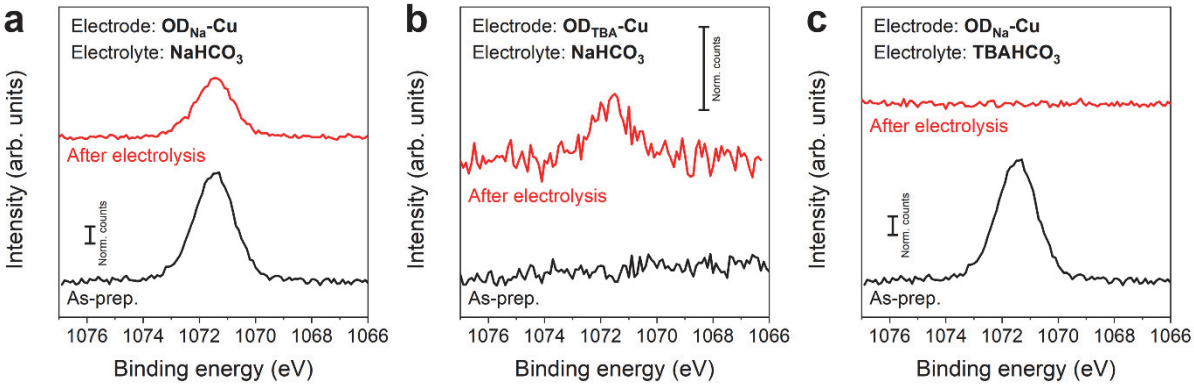

Supplementary Fig. 21 | XPS Na 1*s* spectra of OD-Cu after pulsed CO_2 electrolysis. XPS Na 1*s* spectra of OD-Cu samples before and after 12 h pulsed electrolysis between 0.6 (3 s) and −0.5 (7 s) V_{RHE} in CO_2-saturated electrolytes: **a**, OD_{Na}-Cu electrode in $NaHCO_3$ electrolyte, **b**, OD_{TBA}-Cu electrode in $NaHCO_3$ electrolyte, and **c**, OD_{Na}-Cu electrode in $TBAHCO_3$ electrolyte. A scale bar is included to compare the Na 1*s* peak intensities across the Cu samples.

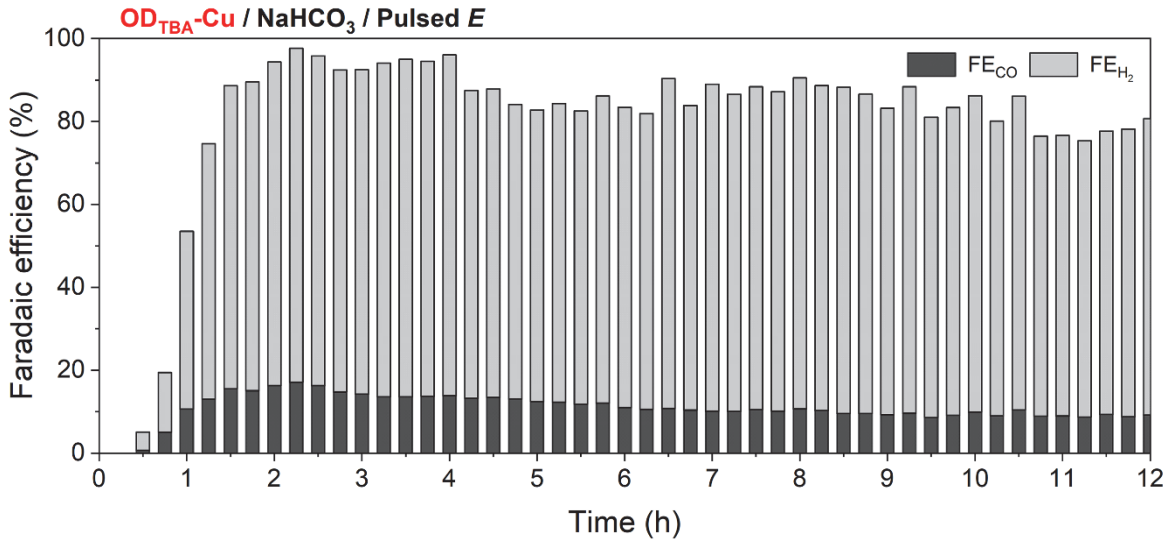

Supplementary Fig. 22 | Pulsed electrolysis of CO_2 to CO on OD_{TBA}-Cu. Faradaic efficiencies for CO and H_2 production on OD_{TBA}-Cu for 12 h pulsed electrolysis between 0.6 (3 s) and −0.5 (7 s) V_{RHE} in a CO_2-saturated 0.1 M $NaHCO_3$ electrolyte.

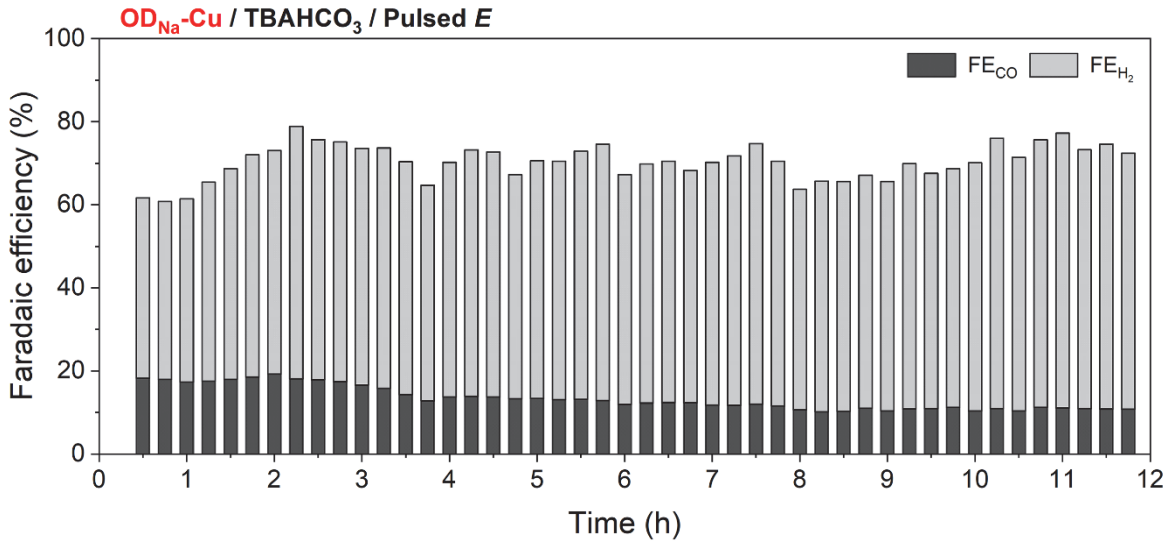

Supplementary Fig. 23 | Pulsed electrolysis of CO_2 to CO on OD_{Na}-Cu in $TBAHCO_3$ electrolyte. Faradaic efficiencies for CO and H_2 production on OD_{Na}-Cu for 12 h pulsed electrolysis between 0.6 (3 s) and −0.5 (7 s) V_{RHE} in a CO_2-saturated 0.1 M $TBAHCO_3$ electrolyte.

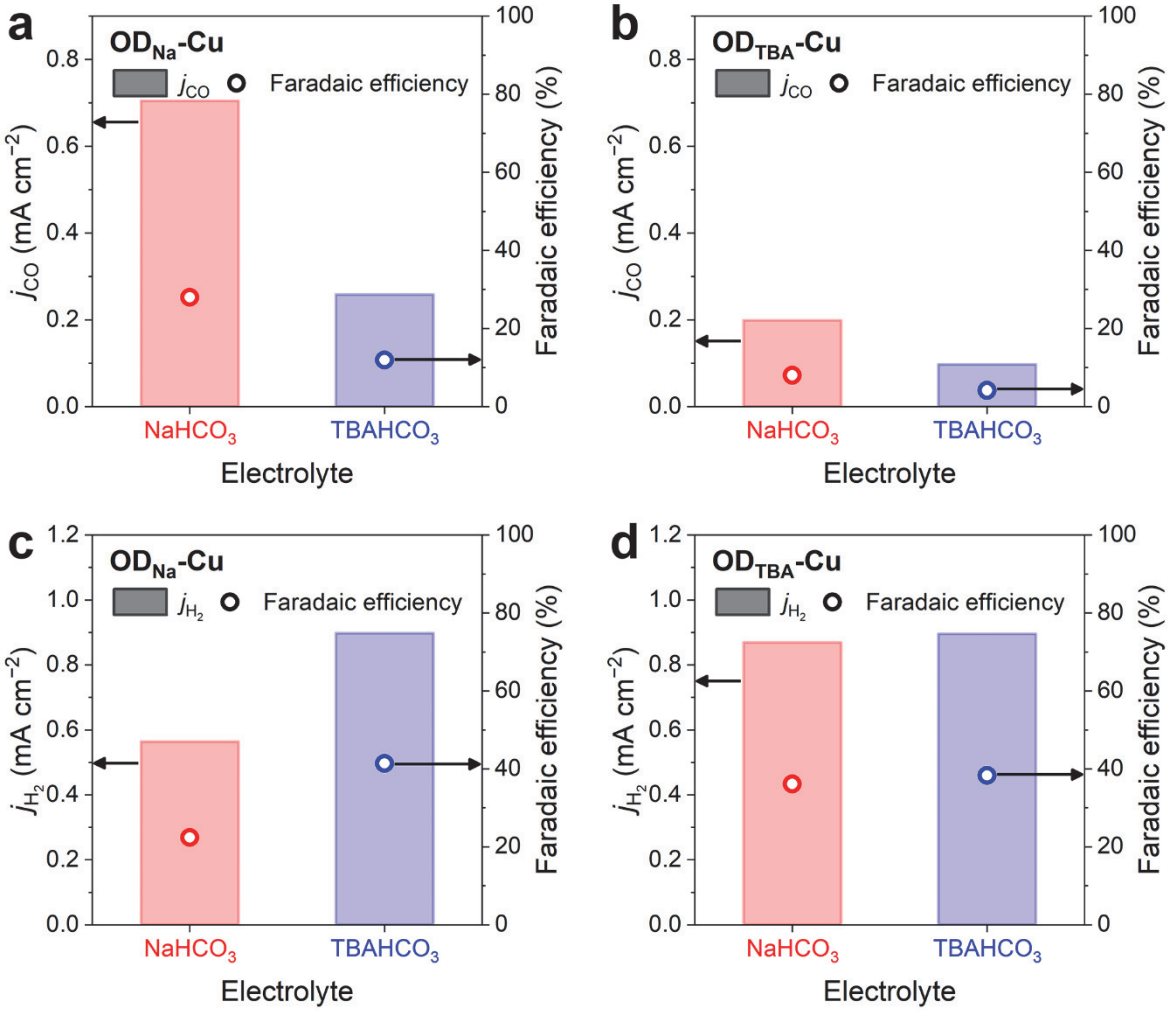

Supplementary Fig. 24 | Influence of cation identity in electrolyte on CO_2RR. Initial partial current densities and Faradaic efficiencies for **a,b**, CO and **c,d**, H_2 production on OD_{Na}-Cu (**a,c**) and OD_{TBA}-Cu (**b,d**) at −0.5 V_{RHE}. The electrolytes were CO_2-saturated 0.1 M $NaHCO_3$ and $TBAHCO_3$.

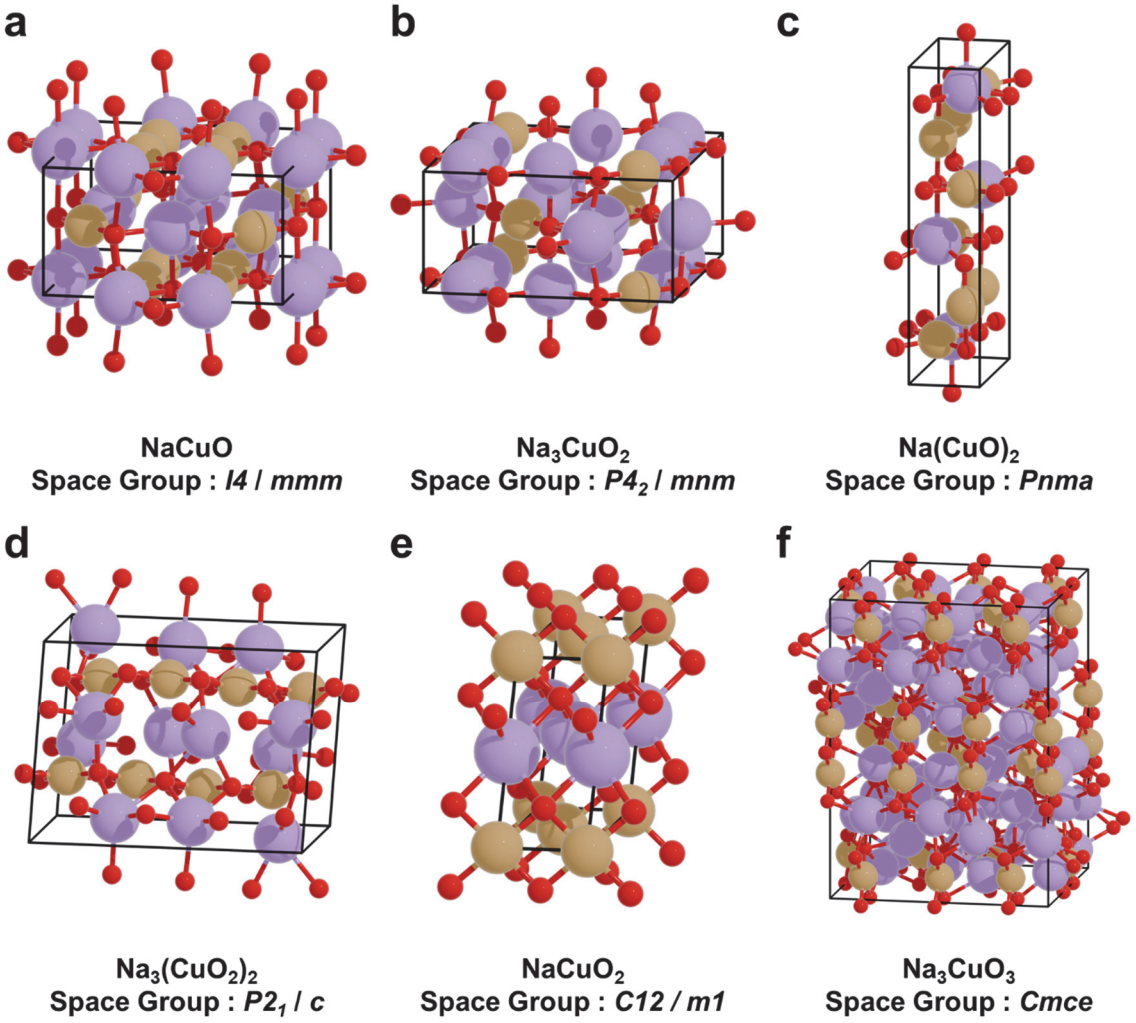

Supplementary Fig. 25 | Crystal structures of selected Na-Cu-O compounds. Conventional unit cell representations of bulk **a**, NaCuO, **b**, Na_3CuO_2, **c**, $Na(CuO)_2$, **d**, $Na_3(CuO_2)_2$, **e**, $NaCuO_2$, and **f**, Na_3CuO_3. The corresponding space group for each compound is indicated below the structure. Na, Cu, and O atoms are represented by purple, yellow, and red balls, respectively. Thermodynamically most stable and structurally well-defined Na-Cu-O compounds were selected based on previously reported DFT-derived phase diagrams.[8-12]

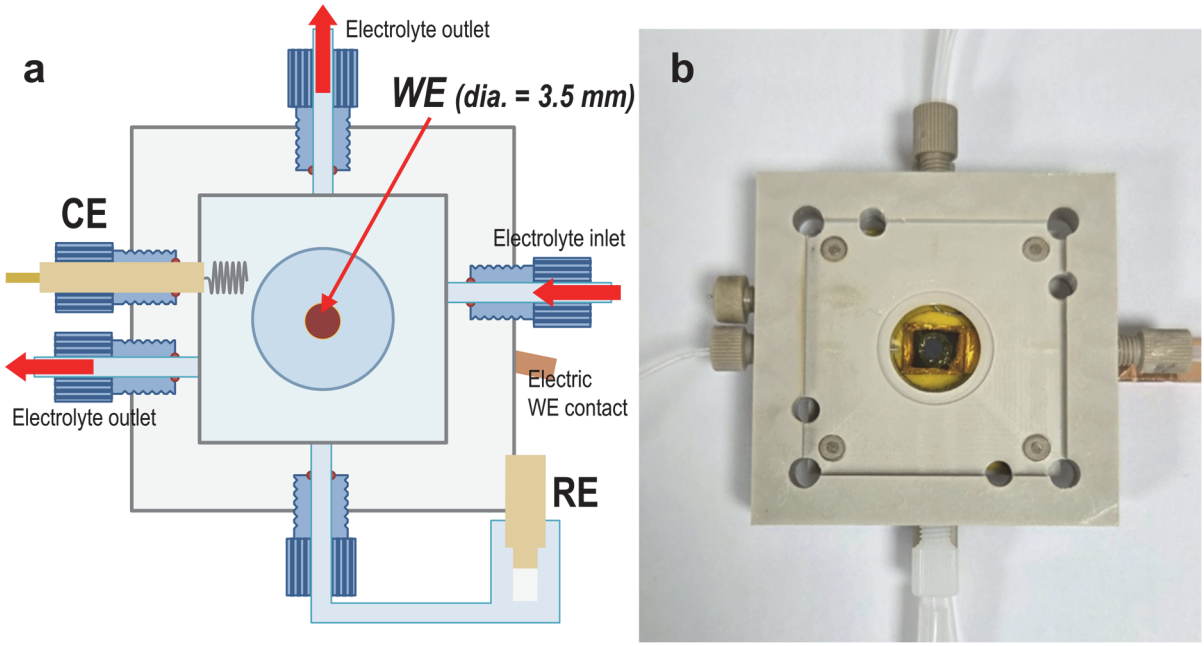

Supplementary Fig. 26 | Electrochemical cell used for Raman spectroscopy studies. a, Schematic and **b**, photographic images of the homemade batch-type electrochemical cell designed for *in situ* Raman spectroscopy measurements.

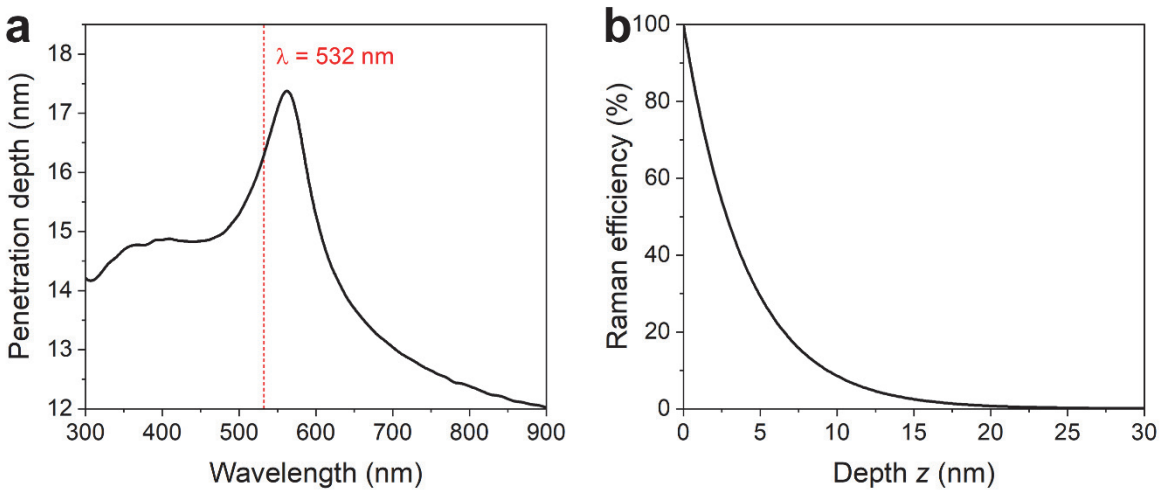

Supplementary Fig. 27 | Calculated Raman efficiency of Cu near surface. a, Simulated penetration depth profile of incident light in Cu at various excitation wavelengths. The red dotted line indicates 532 nm, which lies near the electronic resonance of Cu. **b**, Calculated depth-dependent Raman efficiency under 532 nm excitation. The relative Raman efficiency is normalized to 100% at the Cu surface (depth $z = 0$).

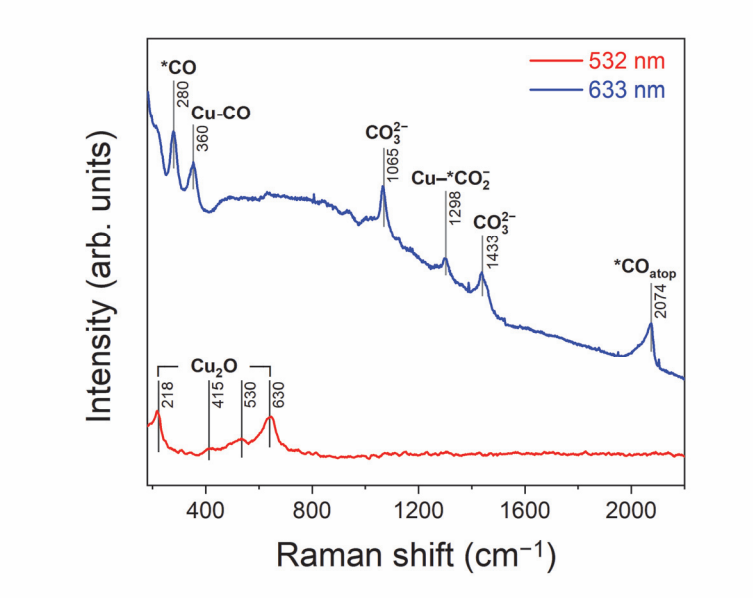

Supplementary Fig. 28 | *In situ* Raman spectra measured under 532 and 633 nm excitations. *In situ* Raman spectra of OD_{Na}-Cu measured at −0.5 V_{RHE} in a CO_2-saturated 0.1 M $NaHCO_3$ electrolyte, obtained using 532 and 633 nm laser excitations. The strong peaks from CO_2RR intermediates are due to chemical enhancement effect by π-backbonding interactions between Cu and adsorbates.[13,14]

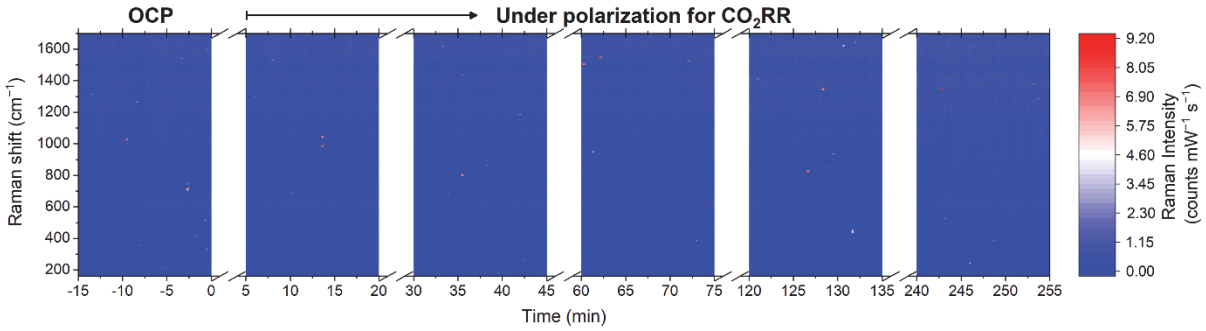

Supplementary Fig. 29 | *In situ* Raman spectra of m-Cu. *In situ* Raman spectra of m-Cu measured at −0.5 V_{RHE} in a CO_2-saturated 0.1 M $NaHCO_3$ electrolyte under 532 nm laser excitation. To minimize undesirable damage to the electrode surface during prolonged operation, spectra were sequentially collected at OCP, and after 5, 30, 60, 120, and 240 min of electrolysis, with each acquisition lasting 15 min.

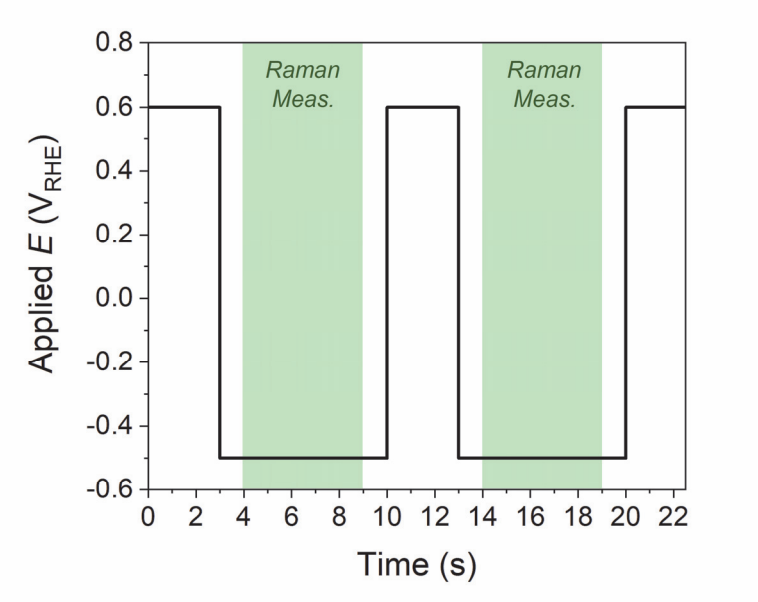

Supplementary Fig. 30 | Collection of *in situ* Raman spectra during pulsed electrolysis. *In situ* Raman spectra were collected during each 7 s cathodic pulse at −0.5 V_{RHE}, starting 1 s after the potential sweep from 0.6 V_{RHE}, with a 5 s acquisition window. This protocol ensured that the spectra were recorded exclusively under cathodic bias.

Supplementary Table 1 | Cryo-APT analysis of the samples. Summary of atomic compositions of the prepared Cu and OD-Cu electrodes measured before and after CO_2RR.

Sample	Condition	Cu[a]	C[b]	N	O	Li	Na	Cs
m-Cu	As prep.	99.925 ± 0.001	0.004		0.072 ± 0.001			
Cu oxide	As prep.	60.047 ± 0.016	0.055 ± 0.001		39.953 ± 0.016			
OD_{Na}-Cu	As prep.	97.466 ± 0.003	0.246 ± 0.001		1.683 ± 0.003		0.607 ± 0.002	
	Aft. static E[c]	97.430 ± 0.003	0.064 ± 0.001		2.454 ± 0.003		0.053 ± 0.001	
	Aft. pulsed E[d]	92.526 ± 0.006	0.108 ± 0.001		6.863 ± 0.006		0.494 ± 0.002	
m-Cu-R	As prep.	99.775 ± 0.002	0.008		0.216 ± 0.002			
OD_{TBA}-Cu	As prep.	98.035 ± 0.002	0.242 ± 0.001		1.680 ± 0.002			
OD_{Li}-Cu	As prep.	98.056 ± 0.006	0.233 ± 0.002		1.129 ± 0.003	0.235 ± 0.003	0.006	
OD_{Cs}-Cu	As prep.	96.316 ± 0.006	0.517 ± 0.002		1.969 ± 0.003			0.585 ± 0.003

[a]The unit of atomic composition is at.%. [b]Carbon impurities, which were attributed to background contamination introduced from APT specimen preparation. [c]APT measurement was conducted after 6 h of CO_2 electrolysis at −0.5 V_{RHE} in CO_2-saturated 0.1 M $NaHCO_3$ electrolyte. [d]APT measurement was conducted after 12 h of pulsed CO_2 electrolysis in CO_2-saturated 0.1 M $NaHCO_3$ electrolyte, where Cu electrode was alternatively polarized between 0.6 (3 s) and −0.5 (7 s) V_{RHE}. A trace amount of Ca was detected in the samples, likely originating from the deionized water used, which contained residual Ca (a common mineral in German-sourced water) despite purification. The H content is not included in this table because accurate quantification requires depth-profile analysis to distinguish genuine H incorporation from background signals.

Supplementary References

1 Ringe, S. *et al.* Understanding Cation Effects in Electrochemical CO_2 Reduction. *Energy Environ. Sci.* **12**, 3001-3014 (2019).

2 Monteiro, M. C. O. *et al.* Absence of CO_2 Electroreduction on Copper, Gold and Silver Electrodes without Metal Cations in Solution. *Nat. Catal.* **4**, 654-662 (2021).

3 Shin, S.-J. *et al.* A Unifying Mechanism for Cation Effect Modulating C1 and C2 Productions from CO_2 Electroreduction. *Nat. Commun.* **13**, 5482 (2022).

4 Monteiro, M. C. O., Dattila, F., López, N. & Koper, M. T. M. The Role of Cation Acidity on the Competition between Hydrogen Evolution and CO_2 Reduction on Gold Electrodes. *J. Am. Chem. Soc.* **144**, 1589-1602 (2022).

5 Weng, S., Toh, W. L. & Surendranath, Y. Weakly Coordinating Organic Cations Are Intrinsically Capable of Supporting CO_2 Reduction Catalysis. *J. Am. Chem. Soc.* **145**, 16787-16795 (2023).

6 Xu, Y., Qiu, Y., Xiao, H. & Xu, B. Deconvolute the Impact of Microenvironment on Proton-Coupled Electron Transfers at Electrochemical Interfaces. *ChemRxiv* (2025). https://doi.org:10.26434/chemrxiv-2025-n2sxg

7 Marcandalli, G., Monteiro, M. C. O., Goyal, A. & Koper, M., T. M. Electrolyte Effects on CO_2 Electrochemical Reduction to CO. *Acc. Chem. Res.* **55**, 1900-1911 (2022).

8 The Materials, P. Materials Data on Na_3CuO_2 by Materials Project. (2020). https://doi.org:/10.17188/1306427

9 The Materials, P. Materials Data on Na_3CuO_3 by Materials Project. (2020). https://doi.org:/10.17188/1292310

10 The Materials, P. Materials Data on NaCuO by Materials Project. (2020). https://doi.org:/10.17188/1288472

11 The Materials, P. Materials Data on $Na_3(CuO_2)_2$ by Materials Project. (2020). https://doi.org:/10.17188/1289443

12 The Materials, P. Materials Data on $Na(CuO)_2$ by Materials Project. (2020). https://doi.org:/10.17188/1272607

13 Lewis, S. P. & Rappe, A. M. Substrate-Adsorbate Coupling in CO-Adsorbed Copper. *Phys. Rev. Lett.* **77**, 5241-5244 (1996).

14 Zhang, Y. *et al.* Electronic Metal-Support Interaction Modulates Cu Electronic Structures for CO_2 Electroreduction to Desired Products. *Nat. Commun.* **16**, 1956 (2025).